

Article

# Single-Phase $\theta$ -Fe<sub>3</sub>C Derived from Prussian Blue and Its Catalytic Application in Fischer-Tropsch Synthesis

Wei Zhang <sup>1,2</sup>, Caiping Ma <sup>1,2,3</sup>, Xingwu Liu <sup>1,4</sup>, Yong Yang <sup>1,4</sup>, Yongwang Li <sup>1,4</sup> and Xiaodong Wen <sup>1,4,\*</sup>

<sup>1</sup> State Key Laboratory of Coal Conversion, Institute of Coal Chemistry, Chinese Academy of Sciences, Taiyuan 030001, China

<sup>2</sup> University of Chinese Academy of Sciences, Beijing 100049, China

<sup>3</sup> College of Chemical Engineering and Technology, Taiyuan University of Technology, Taiyuan 030024, China

<sup>4</sup> National Energy Center for Coal to Liquids, Synfuels China Co., Ltd., Huairou District, Beijing 101400, China

\* Correspondence: wxd@sxicc.ac.cn

**Abstract:** Elucidation of the intrinsic catalytic principle of iron carbides remains a substantial challenge in iron-catalyzed Fischer-Tropsch synthesis (FTS), due to possible interference from other Fe-containing species. Here, we propose a facile approach to synthesize single-phase  $\theta$ -Fe<sub>3</sub>C via the pyrolysis of a molecularly defined Fe-C complex (Fe<sub>4</sub>[Fe(CN)<sub>6</sub>]<sub>3</sub>), thus affording close examination of its catalytic behavior during FTS. The crystal structure of prepared  $\theta$ -Fe<sub>3</sub>C is unambiguously verified by combined XRD and MES measurement, demonstrating its single-phase nature. Strikingly, single-phase  $\theta$ -Fe<sub>3</sub>C exhibited excellent selectivity to light olefins (77.8%) in the C<sub>2</sub>-C<sub>4</sub> hydrocarbons with less than 10% CO<sub>2</sub> formation in typical FTS conditions. This strategy further succeeds with promotion of Mn, evident for its wide-ranging compatibility for the promising industrial development of catalysts. This work offers a facile approach for oriented preparation of single-phase  $\theta$ -Fe<sub>3</sub>C and provides an in-depth understanding of its intrinsic catalytic performance in FTS.

**Keywords:**  $\theta$ -Fe<sub>3</sub>C; single phase; Fischer-Tropsch synthesis; Prussian blue analogue



**Citation:** Zhang, W.; Ma, C.; Liu, X.; Yang, Y.; Li, Y.; Wen, X. Single-Phase  $\theta$ -Fe<sub>3</sub>C Derived from Prussian Blue and Its Catalytic Application in Fischer-Tropsch Synthesis. *Catalysts* **2022**, *12*, 1140. <https://doi.org/10.3390/catal12101140>

Academic Editors: Vincenzo Vaiano and Olga Sacco

Received: 29 August 2022

Accepted: 27 September 2022

Published: 29 September 2022

**Publisher's Note:** MDPI stays neutral with regard to jurisdictional claims in published maps and institutional affiliations.



**Copyright:** © 2022 by the authors. Licensee MDPI, Basel, Switzerland. This article is an open access article distributed under the terms and conditions of the Creative Commons Attribution (CC BY) license (<https://creativecommons.org/licenses/by/4.0/>).

## 1. Introduction

Fischer-Tropsch synthesis (FTS) provides a premier route for production of ultra-clean transportation fuels and valuable chemicals upon conversion of syngas, which is readily available from biomass, coal, and shale gas [1–4]. The conversion of syngas into desirable products requires effective catalysts, which are primarily based on transition metal cobalt, ruthenium, and iron (Fe) [5–9]. In particular, Fe-based catalysts are widely used in industrial FTS processes, due to their low cost and tunability on product distribution, and thus gain enormous attention on its fundamental research [5,10–13]. Among these studies, a realization of the intrinsic role of active components was demonstrated to be essential for the rational design and development of effective catalysts [11,12,14]. However, given the fact that the working Fe-based FTS catalysts generally consist of complex species including both iron carbides, oxides, or metallic iron, complicated interactions between these species significantly impede the recognition of their individual contributions to the overall reaction [15]. To date, though iron carbides are generally believed to be active phases in FTS, it remains difficult to uncover their intrinsic working principle in the complex FTS reaction processes, with the interference of other Fe-containing species [16,17]. What is even more challenging is to precisely distinguish the individual contribution of iron carbide phases (such as  $\chi$ -Fe<sub>5</sub>C<sub>2</sub>,  $\epsilon$ -Fe<sub>2.2</sub>C,  $\theta$ -Fe<sub>3</sub>C, etc.), as they usually coexist under practical FTS conditions [11,18,19].

Over past decades, tremendous effort has been devoted to synthesize single-phase iron carbide and study its catalytic application in FTS via excluding possible interference from iron carbides other than itself and other iron-containing components [13,20,21]. Despite the comprehensive understanding of the intrinsic catalytic behavior of  $\chi$ -Fe<sub>5</sub>C<sub>2</sub> and  $\epsilon$ -Fe<sub>2.2</sub>C in

FTS, relevant research about  $\theta$ -Fe<sub>3</sub>C has not been reported yet [22,23]. In fact,  $\theta$ -Fe<sub>3</sub>C was proposed to be more effective to suppress the formation of undesired CH<sub>4</sub> with respect to  $\chi$ -Fe<sub>5</sub>C<sub>2</sub> and  $\varepsilon$ -Fe<sub>2.2</sub>C, as revealed by density functional theory calculations [24]. Recently, excellent selectivity for C<sub>2+</sub> hydrocarbons (~90%) was realized on the  $\theta$ -Fe<sub>3</sub>C-dominated Fe@C catalyst, advocating its potential in FTS application [12]. In addition, a large enhancement in reactivity towards valuable light olefins' formation was also witnessed with increasing content of  $\theta$ -Fe<sub>3</sub>C in a manganese-modified Fe<sub>3</sub>O<sub>4</sub> microsphere catalyst [25]. Nonetheless, to the best of our knowledge, the definitive contribution of  $\theta$ -Fe<sub>3</sub>C within the FTS process reported in the literature was extrapolated from a complex background containing multiple components. As such, it remains urgent and important to prepare single-phase  $\theta$ -Fe<sub>3</sub>C and investigate its catalytic performance under FTS conditions.

Conventionally, iron carbides are obtained by direct carburization of metallic iron or iron oxides under a syngas atmosphere and high temperature, giving rise to a mixture of iron carbides and oxides due to segregation of Fe or carbon [11,26]. Instead of direct carburization, bottom-up strategies such as wet chemical synthesis or the pyrolysis of molecular precursors provide a powerful approach to synthesize transition metal carbides [22,27]. Particularly, the pyrolysis of molecularly defined precursors enables the preparation of size-controllable and homogeneously distributed materials [12,22]. Inspired by these precedents, we propose to construct a ligand-chelated Fe-complex, followed by controllable pyrolysis to carburize Fe with decomposed carbon in the ligand, to prepare target  $\theta$ -Fe<sub>3</sub>C with uniform spatial distribution of C and Fe atoms.

Combined characterization of X-ray diffraction (XRD) and <sup>57</sup>Fe Mössbauer spectroscopy (MES) was used to verify the crystal structure of as-prepared  $\theta$ -Fe<sub>3</sub>C and monitor the phase transition during the pyrolysis of precursors at different temperatures. The catalytic FTS performance of single-phase  $\theta$ -Fe<sub>3</sub>C was carefully evaluated in typical conditions. We envision that this work will offer a useful approach to synthesis single-phase  $\theta$ -Fe<sub>3</sub>C and further provide an in-depth understanding of its intrinsic catalytic performance in FTS, which will pave the road for the development of Fe-based FTS catalysts.

## 2. Results and Discussion

### 2.1. Structure and Morphology of the Precursor

The structures of the precursors were characterized by XRD and <sup>57</sup>Fe MES, respectively. Figure 1a shows the XRD pattern of the precursor. All peaks in the pattern were attributed to Fe<sub>4</sub>[Fe(CN)<sub>6</sub>]<sub>3</sub>·14H<sub>2</sub>O (JCPDS No. 73-0689), indicating that the precursor has high crystallinity and a pure-phase Prussian blue analogue (PBA) structure. A uniform Fe-C chemical environment with approximately equal carbon chemical potential ( $\mu_C$ ) around each Fe atom was constructed in the precursor, which can provide favorable conditions for the formation of single-phase  $\theta$ -Fe<sub>3</sub>C [23]. The MES spectra of the precursor is shown in Figure 1b and the corresponding Mössbauer parameters are shown in Table 1. The Mössbauer spectrum of the precursor was fitted with two doublets. The pink doublet corresponds to Fe<sup>2+</sup> (IS = 0.72 mm/s, QS = 0.16 mm/s, 35.7%) and the orange doublet correspond to Fe<sup>3+</sup> (IS = 0.00 mm/s, QS = -0.26 mm/s, 64.3%). To further investigate the morphology of the precursor, the precursor was characterized by SEM (Figure 1c,d). It can be clearly observed that precursors were in an extremely uniform rod shape.

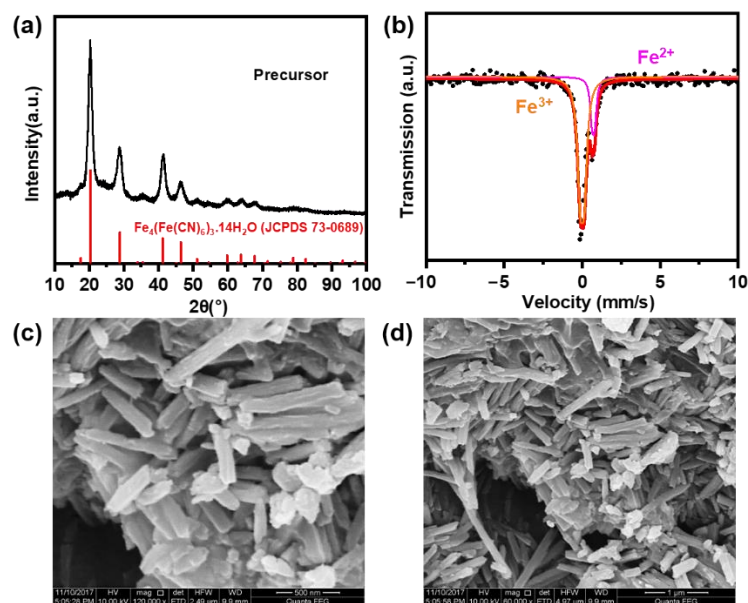


**Figure 1.** The structure and morphology of the precursor: (a) XRD pattern, (b) MES pattern measured at room temperature, (c,d) SEM images.

**Table 1.** MES parameters of the precursor.

Phases	Area (%)	IS (mm/s)	QS (mm/s)
Fe <sup>2+</sup>	35.7	0.72	0.16
Fe <sup>3+</sup>	64.3	0.00	−0.26

## 2.2. Synthesis of $\theta$ -Fe<sub>3</sub>C Catalyst

Pyrolysis temperature and atmosphere play important roles in controlling the phase formed. Theoretical studies showed that low  $\mu_C$  is beneficial to the formation of  $\theta$ -Fe<sub>3</sub>C, which can effectively inhibit the formation of other carbon-rich iron carbides ( $\chi$ -Fe<sub>5</sub>C<sub>2</sub>, h-Fe<sub>7</sub>C<sub>3</sub>,  $\epsilon$ -Fe<sub>2.2</sub>C, etc.) [23]. In addition, low  $\mu_C$  can also avoid excessive carbon deposition on the sample surface. Therefore, N<sub>2</sub> was selected as the pyrolysis atmosphere to synthesis the  $\theta$ -Fe<sub>3</sub>C sample.  $\theta$ -Fe<sub>3</sub>C is generally prepared at temperatures higher than 400 °C, according to previous reports [12,23,28–30]. In order to obtain a single-phase  $\theta$ -Fe<sub>3</sub>C sample, pyrolysis temperatures over 400 °C (450 °C, 500 °C, 550 °C, 600 °C, and 650 °C) were attempted.

The phase identification and compositions of the prepared samples with different pyrolysis temperatures were analyzed by XRD and MES. The XRD patterns of the samples obtained at different temperatures are shown in Figure 2a. <sup>57</sup>Fe MES is a powerful method for analyzing iron-containing phases, which can accurately identify and quantify amorphous or microcrystalline iron species in samples [31,32]. Figure 2b and Table 2 exhibit the MES patterns and the corresponding Mössbauer parameters of the samples obtained at different pyrolysis temperatures, respectively. It can be seen from Figure 2a that the XRD peaks of the sample obtained at 450 °C were mainly composed of the characteristic diffraction peaks of  $\epsilon$ -Fe<sub>2.2</sub>C, and there were also peaks belonging to h-Fe<sub>7</sub>C<sub>3</sub> at 46.4°, 52.6°, 59.4°, 62.7°, and 83.0°. Therefore, the phase composition of the sample obtained at 450 °C was mainly  $\epsilon$ -Fe<sub>2.2</sub>C and a small amount of h-Fe<sub>7</sub>C<sub>3</sub>. Using MES analysis, it can be found that the content of  $\epsilon$ -Fe<sub>2.2</sub>C in the sample was about 69.5%, and the contents of h-Fe<sub>7</sub>C<sub>3</sub> and the Fe (spm) were 20.2% and 10.3%, respectively. The XRD peaks of the sample prepared at 500 °C consisted of the peaks corresponding to  $\theta$ -Fe<sub>3</sub>C and  $\chi$ -Fe<sub>5</sub>C<sub>2</sub> (Figure 2a). The phase compositions of the sample pyrolyzed at 500 °C were mainly  $\theta$ -Fe<sub>3</sub>C and  $\chi$ -Fe<sub>5</sub>C<sub>2</sub>, and their contents were 55.0% and 40.8%, respectively (Figure 2b). The XRD patterns of the samples obtained at 550 °C, 600 °C, and 650 °C exhibited only the characteristic peaks of  $\theta$ -Fe<sub>3</sub>C and a weak peak of graphitic carbon at 30.5°. In addition, the corresponding MES patterns

also showed the typical sextet pattern of  $\theta$ -Fe<sub>3</sub>C with a hyperfine magnetic field (Hhf) of 206–210 kOe. This indicates that the single-phase  $\theta$ -Fe<sub>3</sub>C can be obtained by pyrolysis of the PBA at 550 °C, 600 °C, and 650 °C. Combined with MES analysis (Figure 2b and Table 2), we found that the contents of  $\theta$ -Fe<sub>3</sub>C in the samples obtained at 550 °C, 600 °C, and 650 °C were 95.4%, 95.0%, and 93.9%, respectively. When the temperature was higher than 550 °C, the content of  $\theta$ -Fe<sub>3</sub>C in the samples tended to decrease with the temperature increasing, which may have been caused by the escape of C at elevated temperatures. Therefore, the optimum temperature for preparing single-phase  $\theta$ -Fe<sub>3</sub>C is 550 °C.

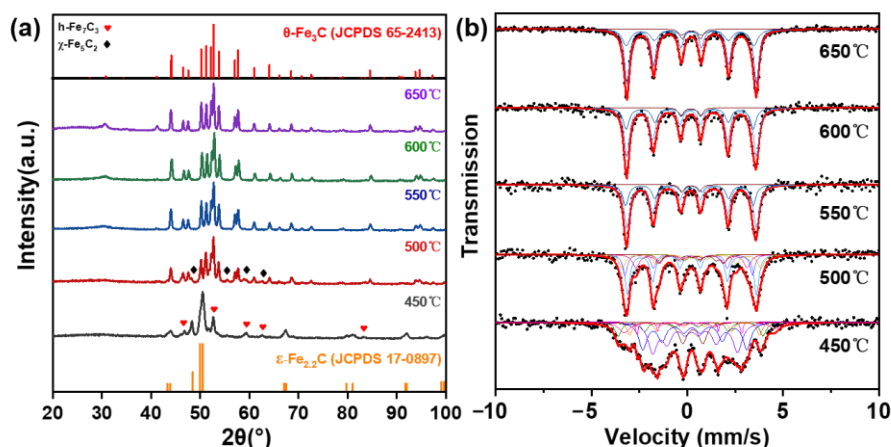


**Figure 2.** Phase identification of prepared samples with different pyrolysis temperatures. (a) XRD patterns. (b) MES patterns measured at room temperature.

**Table 2.** Mössbauer parameters of the catalysts pyrolyzed at different temperatures.

Samples	IS (mm/s)	QS (mm/s)	Hhf (kOe)	Area (%)	Phases	Composition (%)
Sample-450 °C	0.32	0.14	169	26.7	$\epsilon$ -Fe <sub>2.2</sub> C (I)	69.5
	0.07	0.21	235	10.7	$\epsilon$ -Fe <sub>2.2</sub> C (II)	
	0.32	0.18	138	32.1	$\epsilon$ -Fe <sub>2.2</sub> C (III)	
	0.07	0.08	170	3.6	h-Fe <sub>7</sub> C <sub>3</sub> (I)	
	0.37	0.03	211	8.3	h-Fe <sub>7</sub> C <sub>3</sub> (II)	
	−0.14	1.46	246	8.3	h-Fe <sub>7</sub> C <sub>3</sub> (III)	
Sample-500 °C	0.29	1.05	−	10.3	Fe (spm)	10.3
	0.22	0.1	209	36.7	$\theta$ -Fe <sub>3</sub> C (I)	
	0.14	−0.09	207	18.3	$\theta$ -Fe <sub>3</sub> C (II)	
	0.37	−0.23	225	16.3	$\chi$ -Fe <sub>5</sub> C <sub>2</sub> (I)	
	0.24	0.02	180	16.3	$\chi$ -Fe <sub>5</sub> C <sub>2</sub> (II)	
	0.4	−0.3	105	8.2	$\chi$ -Fe <sub>5</sub> C <sub>2</sub> (III)	
Sample-550 °C	0.26	0.82	−	4.2	Fe (spm)	4.2
	0.19	0.07	210	63.6	$\theta$ -Fe <sub>3</sub> C (I)	
	0.17	−0.12	207	31.8	$\theta$ -Fe <sub>3</sub> C (II)	
Sample-600 °C	0.18	−0.92	−	4.6	Fe (spm)	4.6
	0.19	0.07	210	63.3	$\theta$ -Fe <sub>3</sub> C (I)	
	0.17	−0.11	206	31.7	$\theta$ -Fe <sub>3</sub> C (II)	
Sample-650 °C	0.18	−1.01	−	5.0	Fe (spm)	5.0
	0.19	0.03	210	62.6	$\theta$ -Fe <sub>3</sub> C (I)	
	0.15	−0.07	207	31.3	$\theta$ -Fe <sub>3</sub> C (II)	
	0.19	−0.96	−	6.1	Fe (spm)	6.1

### 2.3. Structure and Morphology of the Prepared $\theta$ -Fe<sub>3</sub>C Sample

After optimizing the pyrolysis conditions, the sample pyrolyzed at 550 °C under N<sub>2</sub> for 1 h was further characterized. The phase composition, crystal structure, and crystal size of the prepared sample were verified by XRD and MES. It can be seen from Figure 3a that the XRD pattern of the sample was in good agreement with the standard pure-phase  $\theta$ -Fe<sub>3</sub>C (JCPDS No. 65-2413) and the graphic-carbon (JCPDS No. 41-1487), and no peaks corresponding to other iron-containing phases, indicating that the sample was single-phase

$\theta$ -Fe<sub>3</sub>C. Estimated from the Scherrer equation, the average crystal size of the  $\theta$ -Fe<sub>3</sub>C sample was 32.3 nm. Figure 3b shows the MES spectrum of the  $\theta$ -Fe<sub>3</sub>C sample measured at room temperature and Table 3 is the corresponding Mössbauer parameters. The Mössbauer spectrum was fitted with two sextets and one doublet. The sextet (purple line) with a Hhf value of 210 kOe was assigned to Fe (I) with 12 neighboring iron atoms and the sextet (blue line) with Hhf value of 207 kOe was assigned to Fe (II) with 11 neighboring iron atoms [12,33]. The doublet (orange line) with the IS of 0.19 mm/s and QS of  $-0.96$  mm/s was attributed to the poorly crystalline Fe species in the sample [12]. As shown in Figure 3c,d, the  $\theta$ -Fe<sub>3</sub>C is described within the orthorhombic space group *Pnma* with 12 Fe and 4 C atoms per unit cell. The ideal structure of  $\theta$ -Fe<sub>3</sub>C has two inequivalent crystallographic Fe-sites, named Fe (I) and Fe (II), with an atomic ratio of 2:1. The contents of Fe (I) and Fe (II) in the as-prepared  $\theta$ -Fe<sub>3</sub>C sample were 63.5% and 31.9%, respectively, and their ratio was 1.99, which is very close to the ratio in the ideal structure. It shows that the prepared  $\theta$ -Fe<sub>3</sub>C had good crystallinity. The absence of sextets with Hhf values of  $\sim 329$  kOe assigned to metallic iron, and Hhf values of  $\sim 460$ , 490, and 510 kOe attributed to iron oxides indicates that neither metallic iron nor iron oxides were present [34,35]. This further proves that we have successfully synthesized a single-phase  $\theta$ -Fe<sub>3</sub>C sample.

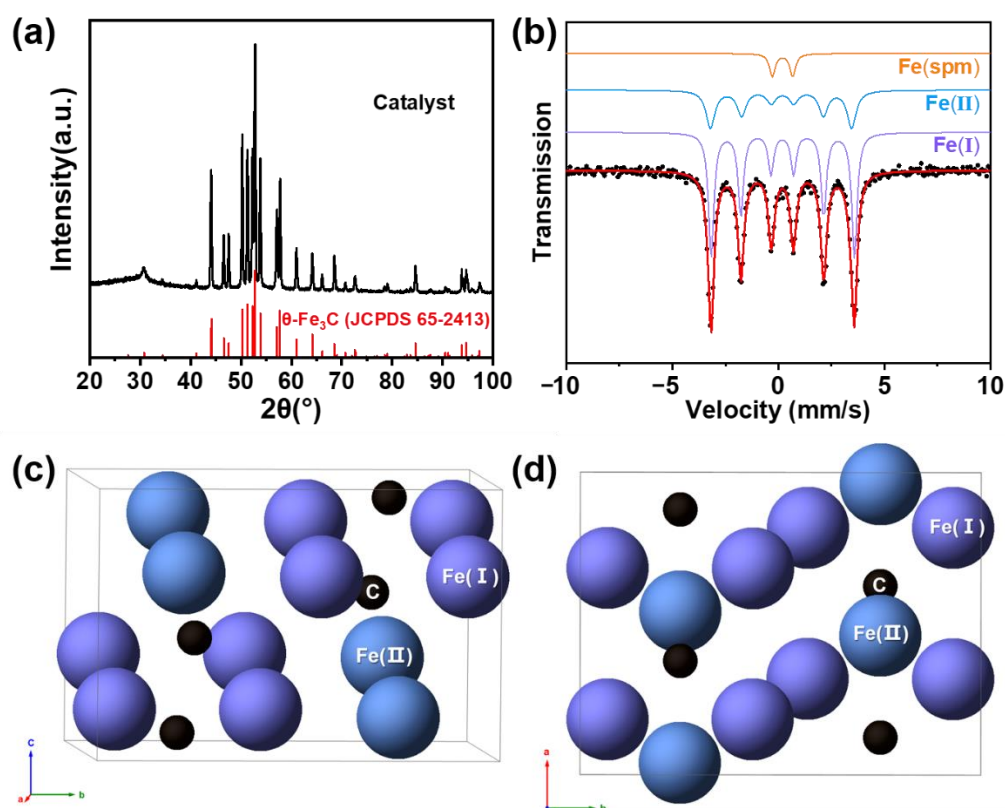


**Figure 3.** The structural identification of prepared single-phase  $\theta$ -Fe<sub>3</sub>C sample. (a) XRD pattern. (b) MES spectra measured at room temperature. (c,d) Crystal structure.

**Table 3.** Mössbauer parameters of the  $\theta$ -Fe<sub>3</sub>C sample.

Phase	Area (%)	IS (mm/s)	QS (mm/s)	Hhf (kOe)
$\theta$ -Fe <sub>3</sub> C (I)	63.5	0.19	0.07	210
$\theta$ -Fe <sub>3</sub> C (II)	31.9	0.17	$-0.12$	207
Fe (spm)	4.6	0.19	$-0.96$	-

The morphology, particle size, and crystal structure of the sample were characterized by TEM. Figure 4 shows the TEM image of the  $\theta$ -Fe<sub>3</sub>C sample. It can be seen from Figure 4a

that the  $\theta$ -Fe<sub>3</sub>C sample presented as random spheres with a particle size of  $33.0 \pm 2.0$  nm, which was consistent with the result estimated by the Scherrer formula (32.3 nm). The  $\theta$ -Fe<sub>3</sub>C particles were wrapped by a carbon shell (Figure 4b,c), which was consistent with the graphitic carbon peak at  $30.5^\circ$  in the XRD pattern. FFT images and interplanar distances of lattice fringes are also frequently used to identify different iron phases. As shown in Figure 4b, the interplanar distance of 3.37 Å in HRTEM corresponded to the (101) plane of  $\theta$ -Fe<sub>3</sub>C. By comparing the FFT image of the sample with the simulated single-crystal diffraction pattern of  $\theta$ -Fe<sub>3</sub>C, the square region in Figure 4c was identified as  $\theta$ -Fe<sub>3</sub>C along with zone axis [1-10] (Figure 4d).

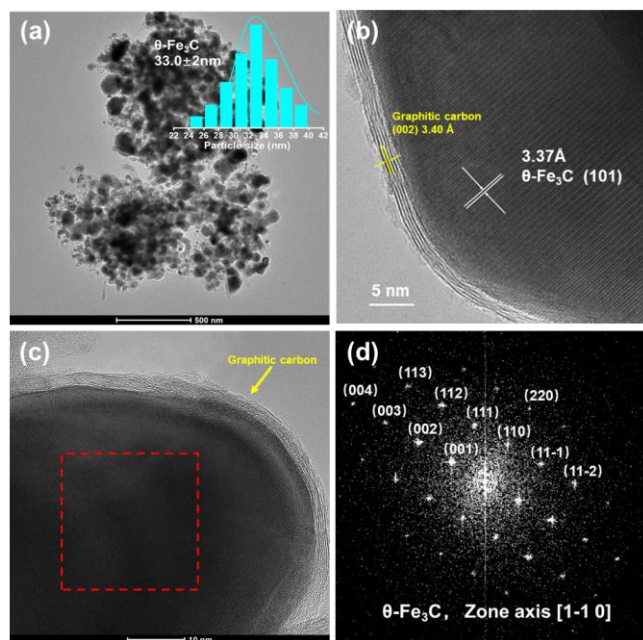


**Figure 4.** (a–c) TEM images of the prepared single-phase  $\theta$ -Fe<sub>3</sub>C sample. Inset histogram in (a) represents size distribution of  $\theta$ -Fe<sub>3</sub>C particles. (d) FFT image of the corresponding selected area marked with red square in (c).

#### 2.4. FTS Performances of the Prepared $\theta$ -Fe<sub>3</sub>C Sample

The most common iron carbides in FTS include  $\epsilon$ -Fe<sub>2.2</sub>C,  $\chi$ -Fe<sub>5</sub>C<sub>2</sub>, and  $\theta$ -Fe<sub>3</sub>C [11,22,36].  $\epsilon$ -Fe<sub>2.2</sub>C and  $\chi$ -Fe<sub>5</sub>C<sub>2</sub> have been synthesized and demonstrated to be active in FTS [13,20,37,38]. There is still a lot of controversy about the role of  $\theta$ -Fe<sub>3</sub>C in FTS. Although there are some reports on the role of  $\theta$ -Fe<sub>3</sub>C in FTS, most of them are based on iron oxide or  $\theta$ -Fe<sub>3</sub>C-dominated catalysts rather than single-phase  $\theta$ -Fe<sub>3</sub>C catalysts. It is unreliable to draw conclusions about the role of  $\theta$ -Fe<sub>3</sub>C based on these systems. Therefore, it is necessary to prepare a single-phase  $\theta$ -Fe<sub>3</sub>C sample and apply it in FTS. The as-prepared  $\theta$ -Fe<sub>3</sub>C sample was applied to FTS reaction under 2.0 MPa, 270 °C, and a H<sub>2</sub>/CO ratio of 2. Notably, the single-phase  $\theta$ -Fe<sub>3</sub>C sample was not subjected to any pretreatment before the reaction, as the purpose of this work is to study the intrinsic catalytic performance of  $\theta$ -Fe<sub>3</sub>C. Figure 5a shows the CO conversion and products selectivity of the  $\theta$ -Fe<sub>3</sub>C sample, and the results are summarized in Table 4. As shown in Figure 5a, the CO conversion of the  $\theta$ -Fe<sub>3</sub>C sample gradually increased from 24% to 30% in the first 40 h, and then kept stable at 30% over prolonged reaction times. With respect to the product distribution, the selectivity of CH<sub>4</sub>, C<sub>2</sub>-C<sub>4</sub>, C<sub>5+</sub> (chains of five carbon atoms and longer) fluctuated slightly in the first 20 h, and remained stable at around 9.4%, 39.4%, and 51.2% after 20 h, respectively. The  $\theta$ -Fe<sub>3</sub>C sample exhibited a stable CO conversion and product selectivity within 100 h of reaction, indicating the excellent catalytic stability of the as-prepared  $\theta$ -Fe<sub>3</sub>C sample. This could be attributed to the core-shell structure of the sample, which not only improves the dispersion of the  $\theta$ -Fe<sub>3</sub>C active phase, but also stabilizes the  $\theta$ -Fe<sub>3</sub>C and protects it from agglomeration during the thermal reaction, which is crucial for

the stability of the activity [12,39]. Overall, the single-phase  $\theta$ -Fe<sub>3</sub>C sample exhibited excellent catalytic performance in terms of stability and selectivity to long-chain hydrocarbons (C<sub>5+</sub>), indicating that  $\theta$ -Fe<sub>3</sub>C possesses superior C-C chain growth ability [12,40]. Furthermore, in the C<sub>2</sub>-C<sub>4</sub> composition range, more valuable olefins accounted for 77.8% of the total C<sub>2</sub>-C<sub>4</sub> products and for 30.6% of all hydrocarbon products, suggesting that  $\theta$ -Fe<sub>3</sub>C is also an ideal catalyst for light olefins. It has been previously reported that  $\theta$ -Fe<sub>3</sub>C can enhance the selectivity of light olefins [25]. The density functional theory (DFT) calculations showed that H<sub>2</sub> can easily form a light-olefin-forming monomer (CH<sub>2</sub> species) on Fe-C hybridization sites of  $\theta$ -Fe<sub>3</sub>C, but the further hydrogenation of CH<sub>2</sub> to CH<sub>3</sub> and CH<sub>4</sub> need to overcome relatively high barriers. This further illustrates that  $\theta$ -Fe<sub>3</sub>C is intrinsically superior in producing light olefins [24,41].

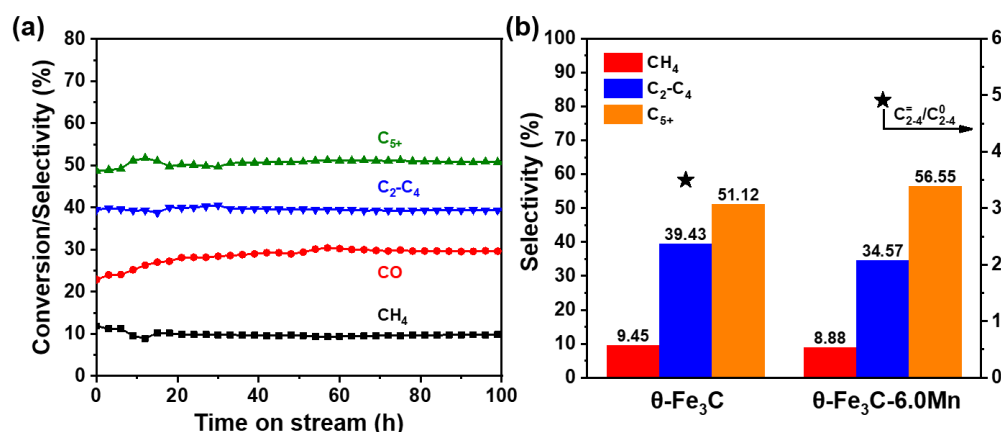


**Figure 5.** FTS performances of catalysts. (a) CO conversion and product selectivity of the  $\theta$ -Fe<sub>3</sub>C sample with the time on stream. (b) Distributions of hydrocarbons over  $\theta$ -Fe<sub>3</sub>C and 6 wt% Mn/Fe<sub>3</sub>C conducted at 270 °C, 2.0 MPa, H<sub>2</sub>/CO = 2, 5000 mL·h<sup>-1</sup>·g<sup>-1</sup>.

**Table 4.** Performance of catalysts in FTS.

	CO Conv. (%)	CO <sub>2</sub> Selec. (C mol%)	HC Distribution (wt%) <sup>2</sup>			C <sub>2-4</sub> <sup>=</sup> /C <sub>2-4</sub> <sup>0</sup>
			CH <sub>4</sub>	C <sub>2</sub> -C <sub>4</sub>	C <sub>5+</sub>	
$\theta$ -Fe <sub>3</sub> C <sup>1</sup>	30	9.9	9.4	39.4	51.2	3.5
6 wt% Mn/Fe <sub>3</sub> C <sup>1</sup>	21.5	14.8	8.8	34.6	56.6	4.9

<sup>1</sup> Reaction conditions: 270 °C, 2.0 MPa, H<sub>2</sub>/CO = 2, 5000 mL·h<sup>-1</sup>·g<sup>-1</sup>. <sup>2</sup> Hydrocarbon distribution was calculated on total hydrocarbons.

Manganese is a commonly used promoter in FTS, which can improve the selectivity of desired products C<sub>5+</sub> and reduce the selectivity of CH<sub>4</sub> [5,42–45]. In order to verify the flexibility of the facile synthetic strategy for preparing the  $\theta$ -Fe<sub>3</sub>C sample in this work, the Mn-doped  $\theta$ -Fe<sub>3</sub>C sample (6 wt% Mn/Fe<sub>3</sub>C) was synthesized by the PBA-mediated synthesis strategy and then applied to the FTS. The XRD pattern of 6 wt% Mn/Fe<sub>3</sub>C is shown in Figure 6, and the texture properties of the samples are summarized in Table S1. It can be seen from Figure 6 that the XRD pattern of 6 wt% Mn/Fe<sub>3</sub>C was consistent with the pure-phase  $\theta$ -Fe<sub>3</sub>C (JCPDS No. 65-2413), indicating that the main phase composition of the sample was  $\theta$ -Fe<sub>3</sub>C. There was no peak attributed to Mn in the XRD pattern, which may be due to the high dispersion and low content of Mn in the sample. As shown in Table S1, the average crystallite size of the 6 wt% Mn/Fe<sub>3</sub>C sample (30.9 nm) was smaller than that of the  $\theta$ -Fe<sub>3</sub>C sample (32.3 nm) and the surface area of the 6 wt% Mn/Fe<sub>3</sub>C sample (142 m<sup>2</sup>/g) was significantly larger than that of the  $\theta$ -Fe<sub>3</sub>C sample (81 m<sup>2</sup>/g). It can be concluded that Mn can enhance the dispersion and favor smaller particles. This was attributed to the stabilization effect caused by the migration of Mn to the surface of the iron particles during the pyrolysis of the precursor (Figure S3). This was consistent with the report that Mn, serving as a structural promoter, improved the dispersion of iron particles, reduced

the crystallite size of iron species, and increased the surface area of the catalysts [44,46,47]. The crystallite size of the 6 wt% Mn/Fe<sub>3</sub>C sample was only slightly reduced, which may be caused by the low content and insufficient dispersion of Mn in the sample [44,46–48]. Figure S6 shows the CO conversion and product selectivity of the 6 wt% Mn/Fe<sub>3</sub>C sample with the time on stream. At the initial state of reaction, compared with that of the  $\theta$ -Fe<sub>3</sub>C sample, the higher CO conversion of the 6 wt% Mn/Fe<sub>3</sub>C sample may have been caused by the more active site provided by a larger surface area. However, under the syngas atmosphere, Mn was constantly separated from the iron particles and enriched on the surface of the iron particles, covering part of the active site of the catalyst [44]. As a result, the CO conversion (21.5%) of the 6 wt% Mn/Fe<sub>3</sub>C sample was lower than that of the single-phase  $\theta$ -Fe<sub>3</sub>C (30%) when the reaction reached the steady state. Therefore, the doping of Mn decreased the activity of the catalyst, which was also observed in previous reports [46,47,49]. Although Mn reduces the activity of the catalyst, it can form an interaction with iron on the surface to improve the selectivity of the catalyst. The performance of the 6 wt% Mn/Fe<sub>3</sub>C sample is summarized in Figure 5b and Table 4. The 6 wt% Mn/Fe<sub>3</sub>C sample exhibited a good C<sub>5+</sub> hydrocarbon selectivity of 56.6% and CH<sub>4</sub> selectivity of 8.8%. Furthermore, the ratio of olefins to alkanes reached 4.9 in the C<sub>2</sub>–C<sub>4</sub> hydrocarbon. Compared with the  $\theta$ -Fe<sub>3</sub>C sample, the 6 wt% Mn/Fe<sub>3</sub>C sample showed a lower methane selectivity, and a higher C<sub>5+</sub> selectivity and ratio of olefins to alkanes (C<sub>2</sub>–C<sub>4</sub>). In the FTS reaction, products' distribution depends on the competition between surface carbon hydrogenation and C–C coupling [50–52]. The addition of Mn can promote C–C coupling and inhibit the hydrogenation process, thereby increasing the selectivity of long-chain hydrocarbons (C<sub>5+</sub>) and reducing the selectivity of light hydrocarbons (CH<sub>4</sub> and C<sub>2</sub>–C<sub>4</sub>). The hydrogenation process is inhibited by Mn, which reduces the selectivity of C<sub>2</sub>–C<sub>4</sub> alkanes and improves the selectivity of C<sub>2</sub>–C<sub>4</sub> alkenes, thereby increasing the ratio of olefins to alkanes (C<sub>2</sub>–C<sub>4</sub>). Therefore, the addition of Mn further improves the  $\theta$ -Fe<sub>3</sub>C selectivity to C<sub>5+</sub> and reduces the selectivity to CH<sub>4</sub>. An improvement in products' distribution has been achieved with promotion of Mn, demonstrating the versatile tunability of the molecularly defined complex pyrolysis strategy that might be applied in practical contexts.

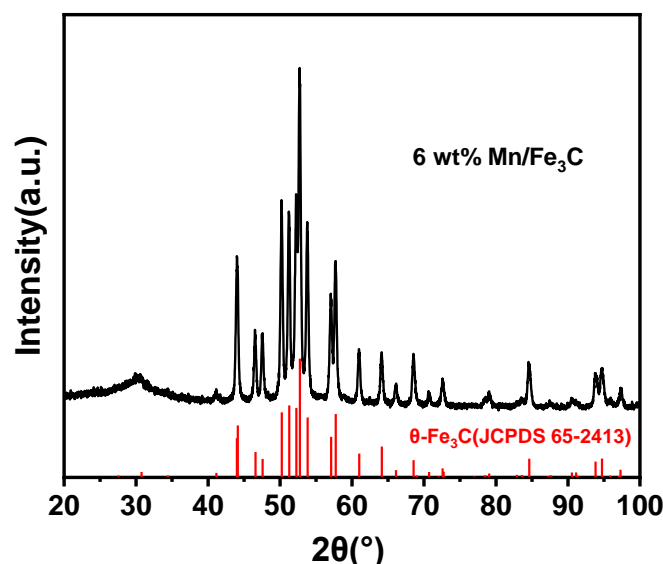


Figure 6. XRD pattern of 6 wt% Mn/Fe<sub>3</sub>C.

### 3. Materials and Methods

#### 3.1. Sample Preparation

To prepare single-phase iron carbide, we modified the procedure reported by Li et al. to synthesize the organometallic precursors with a single-metal Prussian blue analogue (PBA) structure [53]. The precursors (Fe<sub>3</sub>[Fe(CN)<sub>6</sub>]<sub>n</sub>·nH<sub>2</sub>O) were prepared by the reaction

of  $\text{FeCl}_2 \cdot 4\text{H}_2\text{O}$  (Macklin, 99.95%, Shanghai, China) with  $\text{K}_3[\text{Fe}(\text{CN})_6]$  (Macklin, 99.95%) in an aqueous Polyvinylpyrrolidone (PVP) solution. Typically, 6.0 g PVP (Alfa Aesar, M.W. 1,300,000, Waltham, MA, USA) was dissolved in 200 mL deionized water, and 8.95 g  $\text{FeCl}_2 \cdot 4\text{H}_2\text{O}$  was added. Then, 200 mL aqueous  $\text{K}_3[\text{Fe}(\text{CN})_6]$  solution (5 mmol/L) was slowly added into the above solution under vigorous stirring. The resulting dark-blue colloid solution was stirred for a further 0.5 h and aged under dark conditions for 20 h. The obtained precipitates were centrifuged and washed three times with a mixture of ethanol and deionized water, and then dried for 20 h in an oven at 60 °C. Similarly, the  $\text{Mn}_x\text{Fe}_{3-x}[\text{Fe}(\text{CN})_6] \cdot n\text{H}_2\text{O}$  was synthesized by reaction of  $\text{FeCl}_2 \cdot 4\text{H}_2\text{O}$  and  $\text{Mn}(\text{NO}_3)_2 \cdot 4\text{H}_2\text{O}$  (Aladdin, 99.9%, Beijing, China) with  $\text{K}_3[\text{Fe}(\text{CN})_6]$  in aqueous PVP solution. To obtain the  $\text{Fe}_3\text{C}$  and Mn doped  $\text{Fe}_3\text{C}$  catalysts, the obtained  $\text{Fe}_3[\text{Fe}(\text{CN})_6] \cdot n\text{H}_2\text{O}$  and  $\text{Mn}_x\text{Fe}_{3-x}[\text{Fe}(\text{CN})_6] \cdot n\text{H}_2\text{O}$  were pyrolyzed at the desired temperature for 1 h under  $\text{N}_2$ , respectively.

### 3.2. Sample Characterization

X-ray diffraction (XRD) was measured in a D8 powder diffractometer (Bruker, Karlsruhe, Germany) using  $\text{Co K}\alpha$  radiation ( $\lambda = 0.179$  nm) at 35 kV and 40 mA. A continuous mode was used with a scan step of  $0.04^\circ$  and retention time of 0.4 s in the range of  $10\text{--}100^\circ$  for precursors and  $20\text{--}100^\circ$  for catalysts. Mossbauer spectroscopy (MES) was obtained in an MR-351 constant-acceleration Mossbauer spectrometer (FAST, Esslingen, Germany) driven with a triangular reference signal at room temperature. The radioactive source was  $^{57}\text{Co}$  dispersed in a Rh medium. Data analysis was conducted using the MossWinn 4.0 software package. The velocity was calibrated by  $\alpha\text{-Fe}$  foil, and the isomer shift (IS) value was referenced to  $\alpha\text{-Fe}$ . A scanning electron microscopy (SEM) experiment was conducted on FEI 400 Quanta FEG equipment. A transmission electron microscopy (TEM) experiment was conducted on a Talos<sup>TM</sup> 200A (FEI, Portland, OR, USA) electron microscope operated at 200 kV. We dropped the samples dispersed in ethanol by sonication on the copper grid with porous carbon film, and then irradiated the sample with an infrared lamp for 20 min before testing.  $\text{N}_2$  physical adsorption measurement was conducted on Micromeritics ASAP 2420 equipment (Micromeritics, Norcross, GA, USA) at  $-196$  °C. Before analysis, the catalyst was degassed under vacuum at 350 °C for 8 h. The metal concentration of the catalyst was analyzed by inductively coupled plasma-atomic emission spectrometry, and the data were collected and recorded on the Optima 2100D spectrometer (PerkinElmer, Waltham, MA, USA).

### 3.3. FTS Test

The FTS tests were performed on a stainless-steel fixed bed reactor with an isothermal bed length of 5 cm. An amount of 0.5 g catalyst (40–60 mesh) was loaded in the isothermal zone of the reactor and the remaining volume was filled with SiC particles of 60–80 mesh. The reactor system pressure was regulated to 2.0 MPa with syngas ( $\text{H}_2/\text{CO} = 2$ ) at a weight hourly space velocity (WHSV) of 5000 mL/g/h. The solid and liquid phase products were collected by hot trap (160 °C) and a cold trap (0 °C). The tail gas after reaction was divided into two routes, which were measured by wet gas flowmeter and analyzed by gas chromatograph, respectively (Model 6890N and 4890D, Agilent, Santa Clara, CA, USA). The used catalyst after reaction was taken out from the reactor protected by paraffins for further characterization. The mass balance in each test was above 95%.

## 4. Conclusions

In summary, we successfully synthesized single-phase  $\theta\text{-Fe}_3\text{C}$  via the pyrolysis of a molecularly defined  $(\text{Fe}_4[\text{Fe}(\text{CN})_6]_3)$  complex with homogeneous distribution of Fe and C atoms. XRD and MES were employed to verify the crystal structure of prepared  $\theta\text{-Fe}_3\text{C}$ , demonstrating its single-phase nature. On this basis, we carefully examined its catalytic performance in typical FTS conditions by excluding interference from other iron-containing species. Intriguingly, as-prepared single-phase  $\theta\text{-Fe}_3\text{C}$  showed outstanding

light olefins selectivity of 77.8% in C<sub>2</sub>-C<sub>4</sub> hydrocarbons while producing only 9.9% CO<sub>2</sub> upon the overall products, outperforming single-phase Fe<sub>5</sub>C<sub>2</sub> and Fe<sub>2.2</sub>C reported in the literature to date. In addition, improvement in producing olefins was achieved with the promotion of Mn, demonstrating its versatile tunability that might be applied in practical contexts. We anticipate that this work will enrich the understanding of the intrinsic catalytic contribution to the complex FTS process and pave the road for the development of Fe-based FTS catalysts.

**Supplementary Materials:** The following supporting information can be downloaded at: <https://www.mdpi.com/article/10.3390/catal12101140/s1>, Figure S1: SEM images of the  $\theta$ -Fe<sub>3</sub>C sample; Figure S2: SEM images (a) precursor of 6 wt% Mn/Fe<sub>3</sub>C. (b,c) 6 wt% Mn/Fe<sub>3</sub>C sample; Figure S3: TEM elemental mapping images of 6 wt% Mn/Fe<sub>3</sub>C sample; Figure S4: N<sub>2</sub> physisorption isotherm of  $\theta$ -Fe<sub>3</sub>C sample; Figure S5: N<sub>2</sub> physisorption isotherm of 6 wt% Mn/Fe<sub>3</sub>C sample; Figure S6: CO conversion and product selectivity of the 6 wt% Mn/Fe<sub>3</sub>C sample with the time on stream; Table S1: Textural properties, crystallite size, and manganese contents of samples.

**Author Contributions:** Conceptualization, W.Z. and X.W.; methodology, W.Z.; formal analysis, W.Z.; investigation, W.Z., X.L. and C.M.; writing—original draft preparation, W.Z.; writing—review and editing, W.Z. and X.W.; supervision, X.W.; project administration, X.W. and Y.Y.; funding acquisition, Y.L. All authors have read and agreed to the published version of the manuscript.

**Funding:** This work was supported by the National Natural Science Foundation of China (No. 21972157, No. 92045303, No. 21805301, and No. 22172183), CAS Project for Young Scientists in Basic Research (YSBR-005), Key R&D plan of the Beijing Municipal Science and Technology Commission (Z181100005118014), Key Research Program of Frontier Sciences CAS (ZDBS-LY-7007), and CAS Project for Internet Security and Information Technology (CAS-WX2021SF0110).

**Data Availability Statement:** This study did not report any data.

**Acknowledgments:** The authors are grateful for the facilities and financial support from Synfuels China, Co., Ltd. and the Beijing Advanced Innovation Center for Materials Genome Engineering.

**Conflicts of Interest:** The authors declare no conflict of interest.

## References

1. Bao, J.; Yang, G.; Yoneyama, Y.; Tsubaki, N. Significant Advances in C<sub>1</sub> Catalysis: Highly Efficient Catalysts and Catalytic Reactions. *ACS Catal.* **2019**, *9*, 3026–3053. [[CrossRef](#)]
2. Abello, S.; Montane, D. Exploring iron-based multifunctional catalysts for Fischer-Tropsch synthesis: A review. *ChemSusChem* **2011**, *4*, 1538–1556. [[CrossRef](#)] [[PubMed](#)]
3. Dry, M.E. The Fischer-Tropsch process: 1950–2000. *Catal. Today* **2002**, *71*, 227–241. [[CrossRef](#)]
4. Dry, M.E. Present and future applications of the Fischer-Tropsch process. *Appl. Catal. A Gen.* **2004**, *276*, 1–3. [[CrossRef](#)]
5. Xu, Y.; Li, X.; Gao, J.; Wang, J.; Ma, G.; Wen, X.; Yang, Y.; Li, Y.; Ding, M. A hydrophobic FeMn@Si catalyst increases olefins from syngas by suppressing C1 by-products. *Science* **2021**, *371*, 610–613. [[CrossRef](#)] [[PubMed](#)]
6. Torres Galvis, H.M.; Bitter, J.H.; Khare, C.B.; Ruitenbeek, M.; Dugulan, A.I.; de Jong, K.P. Supported iron nanoparticles as catalysts for sustainable production of lower olefins. *Science* **2012**, *335*, 835–838. [[CrossRef](#)]
7. Zhong, L.; Yu, F.; An, Y.; Zhao, Y.; Sun, Y.; Li, Z.; Lin, T.; Lin, Y.; Qi, X.; Dai, Y.; et al. Cobalt carbide nanoprisms for direct production of lower olefins from syngas. *Nature* **2016**, *538*, 84–87. [[CrossRef](#)]
8. Zhang, Y.; Su, X.; Li, L.; Qi, H.; Yang, C.; Liu, W.; Pan, X.; Liu, X.; Yang, X.; Huang, Y.; et al. Ru/TiO<sub>2</sub> Catalysts with Size-Dependent Metal/Support Interaction for Tunable Reactivity in Fischer-Tropsch Synthesis. *ACS Catal.* **2020**, *10*, 12967–12975. [[CrossRef](#)]
9. Zhang, Y.; Yang, X.; Yang, X.; Duan, H.; Qi, H.; Su, Y.; Liang, B.; Tao, H.; Liu, B.; Chen, D.; et al. Tuning reactivity of Fischer-Tropsch synthesis by regulating TiO<sub>x</sub> overlayer over Ru/TiO<sub>2</sub> nanocatalysts. *Nat. Commun.* **2020**, *11*, 3185. [[CrossRef](#)]
10. Wang, D.; Chen, B.; Duan, X.; Chen, D.; Zhou, X. Iron-based Fischer-Tropsch synthesis of lower olefins: The nature of  $\chi$ -Fe<sub>5</sub>C<sub>2</sub> catalyst and why and how to introduce promoters. *J. Energy Chem.* **2016**, *25*, 911–916. [[CrossRef](#)]
11. Chang, Q.; Zhang, C.; Liu, C.; Wei, Y.; Cheruvathur, A.V.; Dugulan, A.I.; Niemantsverdriet, J.W.; Liu, X.; He, Y.; Qing, M.; et al. Relationship between Iron Carbide Phases ( $\epsilon$ -Fe<sub>2</sub>C, Fe<sub>7</sub>C<sub>3</sub>, and  $\chi$ -Fe<sub>5</sub>C<sub>2</sub>) and Catalytic Performances of Fe/SiO<sub>2</sub> Fischer-Tropsch Catalysts. *ACS Catal.* **2018**, *8*, 3304–3316. [[CrossRef](#)]
12. Ma, C.; Zhang, W.; Chang, Q.; Wang, X.; Wang, H.; Chen, H.; Wei, Y.; Zhang, C.; Xiang, H.; Yang, Y.; et al.  $\theta$ -Fe<sub>3</sub>C dominated Fe@C core-shell catalysts for Fischer-Tropsch synthesis: Roles of  $\theta$ -Fe<sub>3</sub>C and carbon shell. *J. Catal.* **2021**, *393*, 238–246. [[CrossRef](#)]
13. Yang, C.; Zhao, H.; Hou, Y.; Ma, D. Fe<sub>5</sub>C<sub>2</sub> nanoparticles: A facile bromide-induced synthesis and as an active phase for Fischer-Tropsch synthesis. *J. Am. Chem. Soc.* **2012**, *134*, 15814–15821. [[CrossRef](#)]

14. Yin, J.; Liu, X.; Liu, X.-W.; Wang, H.; Wan, H.; Wang, S.; Zhang, W.; Zhou, X.; Teng, B.-T.; Yang, Y.; et al. Theoretical exploration of intrinsic facet-dependent CH<sub>4</sub> and C<sub>2</sub> formation on Fe<sub>5</sub>C<sub>2</sub> particle. *Appl. Catal. B Environ.* **2020**, *278*, 119308. [[CrossRef](#)]
15. Opeyemi Otun, K.; Yao, Y.; Liu, X.; Hildebrandt, D. Synthesis, structure, and performance of carbide phases in Fischer-Tropsch synthesis: A critical review. *Fuel* **2021**, *296*, 120689. [[CrossRef](#)]
16. Reymond, J. Changes in the surface structure and composition of an iron catalyst of reduced or unreduced Fe<sub>2</sub>O<sub>3</sub> during the reaction of carbon monoxide and hydrogen. *J. Catal.* **1982**, *75*, 39–48. [[CrossRef](#)]
17. Kuivila, C. Compositional aspects of iron Fischer-Tropsch catalysts: An XPS/reaction study. *J. Catal.* **1989**, *118*, 299–311. [[CrossRef](#)]
18. Butt, J.B. Carbide phases on iron-based Fischer-Tropsch synthesis catalysts part I: Characterization studies. *Catal. Lett.* **1991**, *7*, 61–81. [[CrossRef](#)]
19. Butt, J.B. Carbide phases on iron-based Fischer-Tropsch synthesis catalysts part II: Some reaction studies. *Catal. Lett.* **1991**, *7*, 83–105. [[CrossRef](#)]
20. Xu, K.; Sun, B.; Lin, J.; Wen, W.; Pei, Y.; Yan, S.; Qiao, M.; Zhang, X.; Zong, B. Epsilon-Iron carbide as a low-temperature Fischer-Tropsch synthesis catalyst. *Nat. Commun.* **2014**, *5*, 5783. [[CrossRef](#)]
21. Wezendonk, T.A.; Sun, X.; Dugulan, A.I.; van Hoof, A.J.F.; Hensen, E.J.M.; Kapteijn, F.; Gascon, J. Controlled formation of iron carbides and their performance in Fischer-Tropsch synthesis. *J. Catal.* **2018**, *362*, 106–117. [[CrossRef](#)]
22. Santos, V.P.; Wezendonk, T.A.; Jaen, J.J.; Dugulan, A.I.; Nasalevich, M.A.; Islam, H.U.; Chojecki, A.; Sartipi, S.; Sun, X.; Hakeem, A.A.; et al. Metal organic framework-mediated synthesis of highly active and stable Fischer-Tropsch catalysts. *Nat. Commun.* **2015**, *6*, 6451. [[CrossRef](#)] [[PubMed](#)]
23. Smit, E.D.; Cinquini, F.; Beale, A.M.; Safonova, O.V.; Beek, W.V.; Sautet, P.; Weckhuysen, B.M. Stability and Reactivity of ε-χ-θ Iron Carbide Catalyst Phases in Fischer-Tropsch Synthesis: Controlling μc. *J. Am. Chem. Soc.* **2010**, *132*, 14928–14941. [[CrossRef](#)] [[PubMed](#)]
24. Huo, C.F.; Li, Y.W.; Wang, J.; Jiao, H. Insight into CH<sub>4</sub> formation in iron-catalyzed Fischer-Tropsch synthesis. *J. Am. Chem. Soc.* **2009**, *131*, 14713–14721. [[CrossRef](#)] [[PubMed](#)]
25. Liu, Y.; Chen, J.-F.; Bao, J.; Zhang, Y. Manganese-Modified Fe<sub>3</sub>O<sub>4</sub> Microsphere Catalyst with Effective Active Phase of Forming Light Olefins from Syngas. *ACS Catal.* **2015**, *5*, 3905–3909. [[CrossRef](#)]
26. Niu, L.; Liu, X.; Wen, X.; Yang, Y.; Xu, J.; Li, Y. Effect of potassium promoter on phase transformation during H<sub>2</sub> pretreatment of a Fe<sub>2</sub>O<sub>3</sub> Fischer Tropsch synthesis catalyst precursor. *Catal. Today* **2020**, *343*, 101–111. [[CrossRef](#)]
27. An, B.; Cheng, K.; Wang, C.; Wang, Y.; Lin, W. Pyrolysis of Metal–Organic Frameworks to Fe<sub>3</sub>O<sub>4</sub>@Fe<sub>5</sub>C<sub>2</sub> Core–Shell Nanoparticles for Fischer-Tropsch Synthesis. *ACS Catal.* **2016**, *6*, 3610–3618. [[CrossRef](#)]
28. Wang, X.; Zhang, P.; Wang, W.; Lei, X.; Yang, H. Fe<sub>3</sub>C and Mn doped Fe<sub>3</sub>C nanoparticles: Synthesis, morphology and magnetic properties. *RSC Adv.* **2015**, *5*, 57828–57832. [[CrossRef](#)]
29. Barman, B.K.; Nanda, K.K. Prussian blue as a single precursor for synthesis of Fe/Fe<sub>3</sub>C encapsulated N-doped graphitic nanostructures as bi-functional catalysts. *Green Chem.* **2016**, *18*, 427–432. [[CrossRef](#)]
30. Wang, X.; Zhang, P.; Gao, J.; Chen, X.; Yang, H. Facile synthesis and magnetic properties of Fe<sub>3</sub>C/C nanoparticles via a sol-gel process. *Dye. Pigment.* **2015**, *112*, 305–310. [[CrossRef](#)]
31. Niemantsverdriet, J.W.; Flipse, C.F.J.; Van Der Kraan, A.M.; Van Loef, J.J. A Mössbauer study of surface effects on iron Fischer-Tropsch catalysts. *Appl. Surf. Sci.* **1982**, *10*, 302–313. [[CrossRef](#)]
32. Phillips, J. Application of Mössbauer spectroscopy for the characterization of iron-containing catalysts. *Hyperfine Interact.* **1998**, *111*, 3–16. [[CrossRef](#)]
33. Liu, X.W.; Zhao, S.; Meng, Y.; Peng, Q.; Dearden, A.K.; Huo, C.F.; Yang, Y.; Li, Y.W.; Wen, X.D. Mossbauer Spectroscopy of Iron Carbides: From Prediction to Experimental Confirmation. *Sci. Rep.* **2016**, *6*, 26184. [[CrossRef](#)] [[PubMed](#)]
34. Lyubutin, I.S.; Lin, C.R.; Korzhetskiy, Y.V.; Dmitrieva, T.V.; Chiang, R.K. Mössbauer spectroscopy and magnetic properties of hematite/magnetite nanocomposites. *J. Appl. Phys.* **2009**, *106*, 034311. [[CrossRef](#)]
35. Bukur, D.B.; Okabe, K.; Rosynek, M.P.; Li, C.P.; Wang, D.J.; Rao, K.R.P.M.; Huffman, G.P. Activation Studies with a Precipitated Iron Catalyst for Fischer-Tropsch Synthesis. *J. Catal.* **1995**, *155*, 353–365. [[CrossRef](#)]
36. Datye, A.K.; Jin, Y.; Mansker, L.; Motjope, R.T.; Dlamini, T.H.; Coville, N.J. The nature of the active phase in iron Fischer-Tropsch catalysts. *Stud. Surf. Sci. Catal.* **2000**, *130*, 1139–1144.
37. Hong, S.Y.; Chun, D.H.; Yang, J.I.; Jung, H.; Lee, H.T.; Hong, S.; Jang, S.; Lim, J.T.; Kim, C.S.; Park, J.C. A new synthesis of carbon encapsulated Fe<sub>5</sub>C<sub>2</sub> nanoparticles for high-temperature Fischer-Tropsch synthesis. *Nanoscale* **2015**, *7*, 16616–16620. [[CrossRef](#)]
38. Wang, P.; Chen, W.; Chiang, F.K.; Dugulan, A.I.; Song, Y.; Pestman, R.; Zhang, K.; Yao, J.; Feng, B.; Miao, P.; et al. Synthesis of stable and low-CO<sub>2</sub> selective epsilon-iron carbide Fischer-Tropsch catalysts. *Sci. Adv.* **2018**, *4*, eaau2947. [[CrossRef](#)]
39. Yu, G.; Sun, B.; Pei, Y.; Xie, S.; Yan, S.; Qiao, M.; Fan, K.; Zhang, X.; Zong, B. Fe<sub>x</sub>O<sub>y</sub>@C spheres as an excellent catalyst for Fischer-Tropsch synthesis. *J. Am. Chem. Soc.* **2010**, *132*, 935–937. [[CrossRef](#)]
40. Zhang, Q.; Gu, J.; Chen, J.; Qiu, S.; Wang, T. Facile fabrication of porous Fe@C nanohybrids from natural magnetite as excellent Fischer-Tropsch catalysts. *Chem. Commun.* **2020**, *56*, 4523–4526. [[CrossRef](#)]
41. Liu, Y.; Lu, F.; Tang, Y.; Liu, M.; Tao, F.F.; Zhang, Y. Effects of initial crystal structure of Fe<sub>2</sub>O<sub>3</sub> and Mn promoter on effective active phase for syngas to light olefins. *Appl. Catal. B Environ.* **2020**, *261*, 118219. [[CrossRef](#)]
42. Li, J.; Wu, L.; Zhang, S.; Wen, J.; Liu, M.; Wang, C.; Li, X. The promotional effect of Mn on Fe-based Fischer-Tropsch catalysts for the synthesis of C<sub>5+</sub> hydrocarbons. *Sustain. Energy Fuels* **2019**, *3*, 219–226. [[CrossRef](#)]

43. Zhang, Y.; Ma, L.; Wang, T.; Li, X. MnO<sub>2</sub> coated Fe<sub>2</sub>O<sub>3</sub> spindles designed for production of C<sub>5+</sub> hydrocarbons in Fischer-Tropsch synthesis. *Fuel* **2016**, *177*, 197–205. [[CrossRef](#)]
44. Dad, M.; Fredriksson, H.O.A.; Van de Loosdrecht, J.; Thüne, P.C.; Niemantsverdriet, J.W. Stabilization of iron by manganese promoters in uniform bimetallic FeMn Fischer–Tropsch model catalysts prepared from colloidal nanoparticles. *Catal. Struct. React.* **2015**, *1*, 101–109. [[CrossRef](#)]
45. Das, D.; Ravichandran, G.; Chakrabarty, D.K. Conversion of syngas to light olefins over silicalite-1 supported iron and cobalt catalysts: Effect of manganese addition. *Catal. Today* **1997**, *36*, 285–293. [[CrossRef](#)]
46. Tao, Z.; Yang, Y.; Wan, H.; Li, T.; An, X.; Xiang, H.; Li, Y. Effect of manganese on a potassium-promoted iron-based Fischer-Tropsch synthesis catalyst. *Catal. Lett.* **2007**, *114*, 161–168. [[CrossRef](#)]
47. Tao, Z.; Yang, Y.; Zhang, C.; Li, T.; Ding, M.; Xiang, H.; Li, Y. Study of Manganese Promoter on a Precipitated Iron-Based Catalyst for Fischer-Tropsch Synthesis. *J. Nat. Gas Chem.* **2007**, *16*, 278–285. [[CrossRef](#)]
48. Campos, A.; Lohitharn, N.; Roy, A.; Lotero, E.; Goodwin, J.G.; Spivey, J.J. An activity and XANES study of Mn-promoted, Fe-based Fischer–Tropsch catalysts. *Appl. Catal. A Gen.* **2010**, *375*, 12–16. [[CrossRef](#)]
49. Zhang, Y.; Wang, T.; Ma, L.; Shi, N.; Zhou, D.; Li, X. Promotional effects of Mn on SiO<sub>2</sub>-encapsulated iron-based spindles for catalytic production of liquid hydrocarbons. *J. Catal.* **2017**, *350*, 41–47. [[CrossRef](#)]
50. Li, J.; Cheng, X.; Zhang, C.; Yang, Y.; Li, Y. Effects of alkali on iron-based catalysts for Fischer-Tropsch synthesis: CO chemisorptions study. *J. Mol. Catal. A Chem.* **2015**, *396*, 174–180. [[CrossRef](#)]
51. Wang, S.; Yin, Q.; Guo, J.; Ru, B.; Zhu, L. Improved Fischer–Tropsch synthesis for gasoline over Ru, Ni promoted Co/HZSM-5 catalysts. *Fuel* **2013**, *108*, 597–603. [[CrossRef](#)]
52. Govender, N.S.; Botes, F.G.; de Croon, M.H.J.M.; Schouten, J.C. Mechanistic pathway for methane formation over an iron-based catalyst. *J. Catal.* **2008**, *260*, 254–261. [[CrossRef](#)]
53. Li, X.; Yuan, L.; Wang, J.; Jiang, L.; Rykov, A.I.; Nagy, D.L.; Bogdan, C.; Ahmed, M.A.; Zhu, K.; Sun, G.; et al. A “copolymer-co-morphology” conception for shape-controlled synthesis of Prussian blue analogues and as-derived spinel oxides. *Nanoscale* **2016**, *8*, 2333–2342. [[CrossRef](#)] [[PubMed](#)]